

# A first-principles study of the electronic, vibrational, and optical properties of planar SiC quantum dots

Rupali Jindal, Vaishali Roondhe, and Alok Shukla\*

Department of Physics, Indian Institute of Technology Bombay, Powai, Mumbai 400076, India

E-mail: rupalijindalpu@gmail.com, oshivaishali@gmail.com, shukla@iitb.ac.in

**Abstract.** With the reported synthesis of a fully planar 2D silicon carbide (SiC) allotrope, the possibilities of its technological applications are enormous. Recently, several authors have computationally studied the structures and electronic properties of a variety of novel infinite periodic SiC monolayers, in addition to the honeycomb one. In this work, we perform a systematic first-principles investigation of the geometry, electronic structure, vibrational, and optical absorption spectra of several finite, but, fully planar structures of SiC, i.e., 0D quantum dots (QDs). The sizes of the studied structures are in the 1.20–2.28 nm range, with their computed HOMO(H)-LUMO(L) gaps ranging from 0.66 eV to 4.09 eV, i.e., from the IR to the UV region of the spectrum. The H-L gaps in the SiC QDs are larger as compared to the band gaps of the corresponding monolayers, confirming the quantum confinement effects. In spite of covalent bonding in the QDs, Mulliken charge analysis reveals that Si atoms exhibit positive charges, whereas the C atoms acquire negative charges, due to the different electron affinities of the two atoms. Furthermore, a strong structure property relationship is observed with fingerprints both in the vibrational and optical spectra. The wide range of H-L gaps in different SiC QDs makes them well-suited for applications in fields such as photocatalysis, light-emitting diodes, and solar cells.

## 1. Introduction

Silicon carbide (SiC) is an interesting wide bandgap bulk semiconductor that has been investigated thoroughly[1, 2, 3] because of its numerous applications in fields such as bioimaging, photovoltaic cells, optical sensors in the UV region, etc. Its inherent properties like wide band gap, chemical inertness,[3, 4] and high thermal conductivity[5, 6, 7] make it suitable for devices operating at high temperature, frequency, and voltage such as power electronic devices[8, 9, 10]. In the crystalline form, SiC exists in over 250 polytypes[11, 12] although the most frequently used polytypes for device applications have cubic (e.g., 3C-SiC), hexagonal (e.g., 2H-SiC, 4H-SiC, 6H-SiC), and rhombohedral (e.g., 15R-SiC) crystal structures. Interestingly, each of these polytypes with different electronic, optical, and vibrational properties has been widely explored both experimentally, and theoretically.[13, 14, 15, 16, 17, 18, 19, 20] Over and above these properties, it is worth mentioning that SiC is an environmental friendly material which can be produced economically as both Si and C are abundant elements on earth.

The optical spectra of all the polytypes of SiC lie between 2.416 to 3.33 eV, but, n-type doping modifies its optical bands to 1-3 eV region [21]. However, bulk SiC polytypes show weak luminescence characteristics because of their indirect bandgap [17]. In the present times, there is a continuous effort to miniaturize devices to the nanoscale with the aim of tailoring the material properties by exploiting the quantum size effects. It is well-known that the electronic and optical properties of matter alter considerably when its dimensionality is reduced, and can also result in enhanced photoluminescence of otherwise poorly luminescent materials. With the aim of understanding the influence of reduced dimensionality on its properties, various nanostructures of SiC such as one-dimensional (1D) nanowires[22, 23, 24, 25], 1D nanotubes [26, 27, 28, 25], nanoribbons [29], and porous and other complex nanostructures [30, 31, 32, 33] have been synthesized successfully. Furthermore, nanosized SiC compound clusters, which can be seen as precursors of SiC QDs, were produced in the gas phase using the laser vaporization technique and deposited on various substrates by Melinon *et al.*[34] In our group, first-principles density-functional theory (DFT) studies on SiC nanoribbons of both armchair and zigzag varieties to explore their band structures and optical properties have been performed previously[35, 36].

Strong covalent bonding leads to stable SiC structures even in reduced dimensions. In bulk, SiC with four covalent bonds exhibits  $sp^3$  hybridization forming four  $\sigma$  bonds, whereas SiC monolayer, due to its planar nature displays  $sp^2$  hybridization forming three  $\sigma$  bonds, while the remaining  $p_z$  orbital laterally overlaps with the neighbouring  $p_z$  orbitals, forming a  $\pi$ -electron band. It has been difficult to isolate graphene-like monolayer of SiC because in the bulk form, there is no graphitic phase of SiC held together by Van der Waals forces. All the bulk polytypes of SiC have strong covalent bonds because of which it is difficult to isolate a monolayer by exfoliation methods. However, in remarkable recent works, Chabi *et al.*[37] reported the synthesis of a fully planar graphene-like honeycomb monolayer of SiC by employing a wet exfoliation method, while Polley *et al.*[38] synthesized it on a substrate using a bottom-up approach.

Now that both 1D (nanotubes, nanowires, etc.) and 2D periodic structures of SiC have been synthesized, one wonders if its finite 0D structures, i.e., quantum dots (QDs) can also be synthesized in a controlled manner with tailor-made properties. Because of their 0D (finite) nature, QDs have numerous fascinating properties, as compared to the higher-dimensional structures made of the same material. These include edge effects, tunable energy gaps, efficient photoluminescence, and strong absorption so that their practical implications can be seen all around, such as in solar cells [39, 40, 41, 42], electronic devices[43, 44, 45], light emitting diodes (LEDs) [46, 47, 48, 49, 50, 51, 52], energy storage and conversion[53], etc. Two recent works involving the synthesis of SiC-QDs have been reported: (a) Cao *et al.* [54] synthesised strictly monolayer SiC-QDs of graphitic structures exhibiting intense photoluminescence, while (b) Mizuno *et al.*[55] created SiC-QDs of 3D structures exhibiting  $sp^3$  hybridization. In addition to the widely studied graphitic SiC monolayer, in recent years several novel 2D monolayers of SiC have been proposed based on first-principles calculations[56, 57, 58]. Graphene quantum dots (GQDs) possess remarkable properties such as biocompatibility, low toxicity, and chemical stability, making them strong candidates for sensing, drug delivery, energy storage and conversion applications[59, 60, 61, 62]. Similarly, SiC QDs find applications in bio-imaging, drug delivery, dental implants, etc.[63] Nevertheless, in the area of optoelectronics SiC-QDs offer several advantages as compared to GQDs. Some experiments have reported somewhat higher quantum yield of SiC QDs (7.95%)[54] as compared to GQDs (6.9%)[64]. Additionally, SiC QDs exhibited extended fluorescence lifetimes of 2.59  $\mu s$ [54], much larger than 7.52  $ns$  measured for GQDs [65], and 4.66  $ns$  for MoS<sub>2</sub> QDs[66]. Higher fluorescence lifetimes of SiC-QDs will not only facilitate their easier detection but also lead to superior performance in imaging applications. Furthermore, larger GQDs have a smaller bandgap, which is unsuitable for higher energy optoelectronics[67]. Although reducing the size of GQDs could potentially address this, experimental challenges make this approach difficult to implement[67, 68]. Because SiC has an inherent band gap due to its hetero-atom character, the gaps of the SiC QDs will always be larger than the corresponding GQDs, making them more suitable for UV-Vis optoelectronic applications[69, 70]. In the present work, we investigate the existence of strictly monolayer SiC-QDs of a variety of structures, in addition to the graphitic ones, using a first-principles methodology. Planar SiC QDs, because of their finite extent, will have reactive dangling bonds on the edges leading to edge reconstructions resulting in highly asymmetric structures. Therefore, we have passivated the edges with the H atoms to make them chemically inert because of which the QDs manage to retain their symmetric shapes. In previous several works, we have studied the electronic structure and optical properties of graphene-derived nanostructures such as graphene nanoribbons as well as quantum dots with H-passivated edges, employing a Pariser-Parr-Pople (PPP) model based semiempirical approach[71, 72, 73]. However, in the present work we have employed a DFT-based first-principles approach, and studied the stability, electronic structure, Raman and optical absorption spectra of six different strictly planar structures of SiC-QDs, for which 2D monolayers have been demonstrated to be stable in the previous works.[56, 57, 58]

The remainder of this article is organized as follows. In the next section, we briefly describe our computational

methodology, followed by a detailed discussion of our results. Finally, we summarize our work and describe the key conclusions.

## 2. Computational Approach

In order to investigate the shape and size effect on the properties of the SiC-QDs six structures are studied (a) Haeck-SiC (b) Circular-SiC (c) Tho-SiC (d) Pho-SiC (e) T1-SiC (f) Triangular-SiC, where the number of non-hydrogen atoms is 32, 24, 36, 72, 28, and 22, respectively (Fig. 1). All the initial structures were taken to be planar and in Figs. 1(b) and 1(f), the hexagons are arranged in circular and triangular geometrical shapes, termed Circular-SiC and Triangular-SiC, respectively. In the haeckelite structure squares are connected with octagons and vice-versa[74, 75]. The Tho and Pho structures were initially proposed by Long *et al.*[58] as 2D-periodic monolayers, while here we are considering their 0D counterparts, i.e., QDs whose nomenclature can be explained as follows: (a) The Tho structure is composed of tetragons (T), hexagons(h), and octagons(o), whereas (b) the Pho structure contains pentagons(P), hexagons (h), and octagons (o)[58]. The structure 1(e) named T1-SiC was first proposed by Qin *et. al.* with reference to the linkage of Si – Si and C – C with Si – C bonds[56]. Of the six QDs considered here, the Circular-SiC and Triangular-SiC have graphitic structures and are SiC counterparts of hydrocarbon molecules coronene, and triangulene, respectively. For all the structures considered here, calculations were performed using the Gaussian16 suite of packages [76], employing a first-principles density functional theory (DFT) [77, 78, 79] based approach. Spin-polarized calculations were performed to investigate the possibility of magnetic ground state for all the considered QDs. The first five SiC QDs were found to be stable in non-magnetic spin-singlet states, whereas the Triangular-SiC QD was found to have a spin-triplet ground state. The construction of initial structures and visualization of the considered QDs has been done using Gaussview6 [80] software.

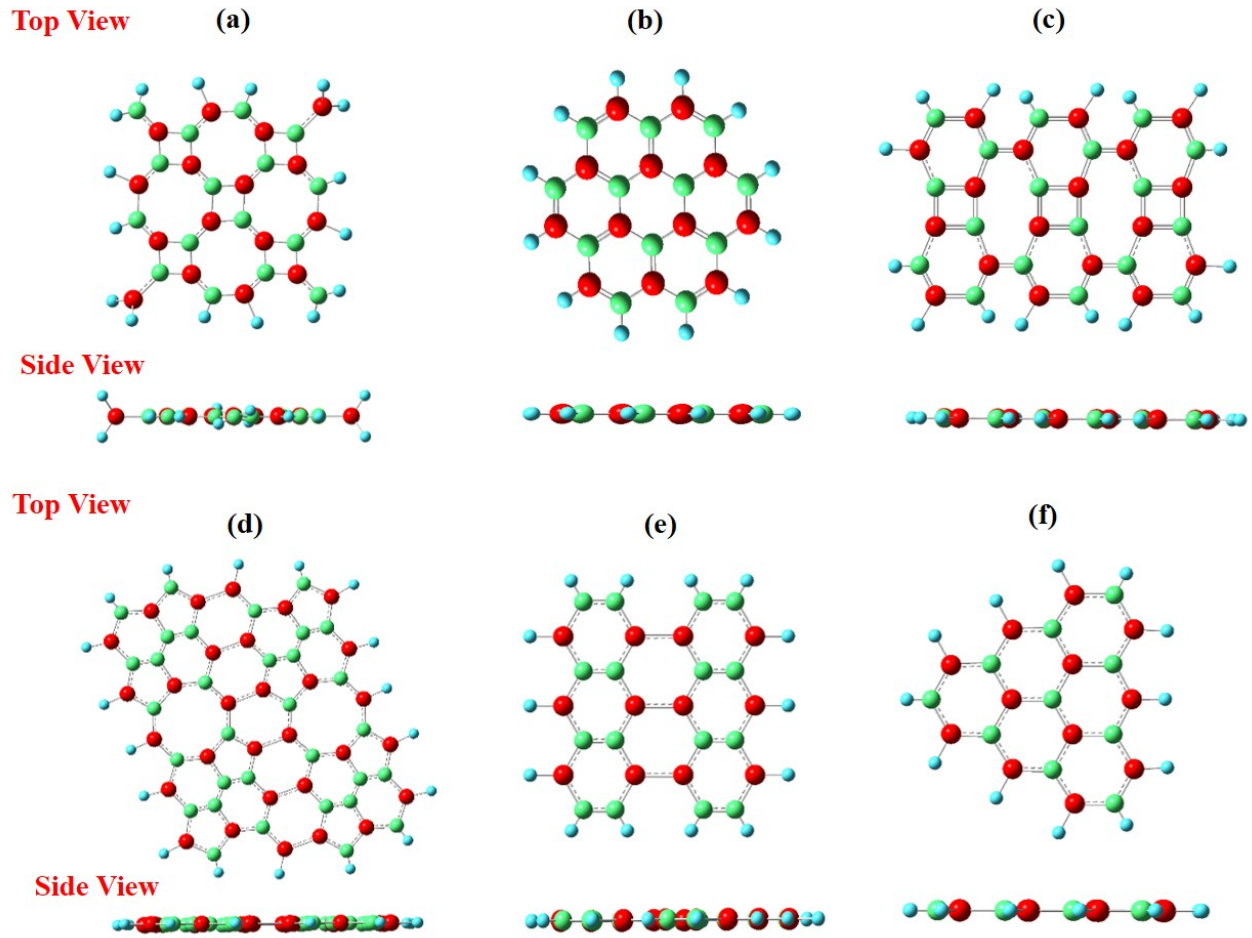


Figure 1: Initial structures of (a) Haack-SiC (b) Circular-SiC (c) Tho-SiC (d) Pho-SiC (e) T1-SiC (f) Triangular-SiC, with silicon, carbon and hydrogen atoms shown in red, green, and blue colors, respectively.

For performing the calculations, the B3LYP hybrid functional coupled with the cc-pvDz basis was used. This functional includes contributions from Becke 88 exchange functional[81], and the correlational functional proposed by Lee, Yang, and Parr[82]. It has been found to perform very well for semiconductors[83], and the QDs considered in this work are semiconducting nanoparticles for which the B3LYP functional is used quite frequently.[84, 85, 86] After performing the geometry optimization, the Raman intensities are calculated for all the structures. The lack of any imaginary vibrational frequencies indicates that the predicted structures of the SiC-QDs are stable. For the Mulliken charge analysis and the calculation of the total and partial density of states multiwfn software is utilized[87]. The optimized structures are used to calculate the optical absorption spectra using the time-dependent density functional theory (TD-DFT), employing the same basis set and functional.

### 3. Results and Discussion

#### 3.1. Structural Parameters

The geometry iterations were performed until the four parameters, namely maximum force, RMS force, maximum displacement, and RMS displacement converged for all the QDs indicating stable structures. In Fig. 2 we present the final optimized geometries of SiC-QDs considered in this work. In the figure, we also indicate the sizes of these QDs, defined as the distances between the farthest hydrogen atoms, and note that they vary in the range of 1.195-2.278 nm. The detailed structural data for each QD, i.e., bond lengths and bond angles, are presented in Tables 1 and 2, respectively.

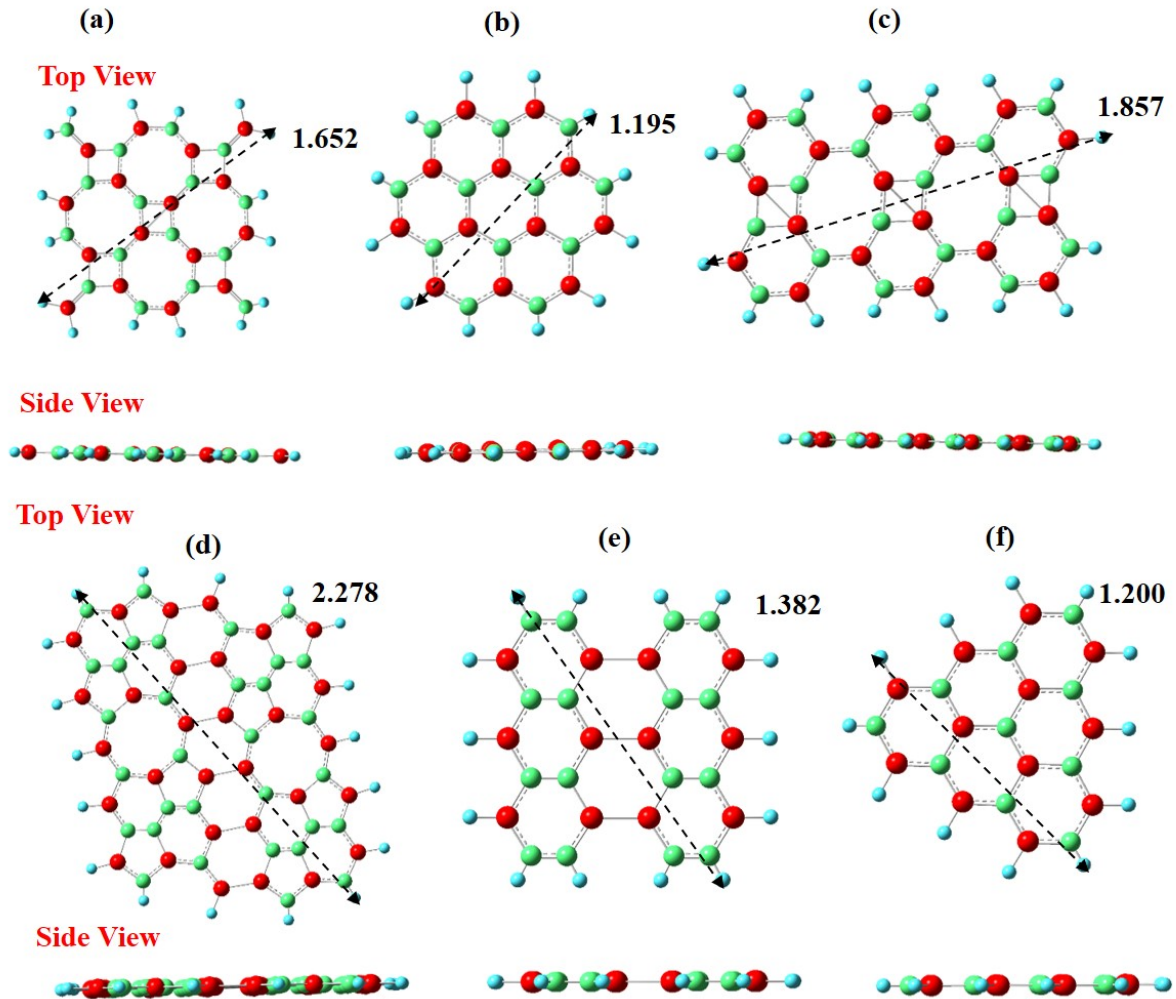


Figure 2: The final optimized structures of (a) Haeck-SiC, (b) Circular-SiC, (c) Tho-SiC, (d) Pho-SiC (e) T1-SiC, and (f) Triangular-SiC, along with their sizes in nm. Silicon, carbon and hydrogen atoms are shown in red, green, and blue colours, respectively.

From the side views of the optimized structures, it is obvious that each QD is strictly planar, implying that each atom contributes one  $p_z$  electron, i.e.,  $\pi$  electron, to the system, while the rest of its three electrons participate in forming  $sp^2$  hybridized  $\sigma$  bonds with its neighbours. The final optimized bond lengths and bond angles show variations from structure to structure.

The Haeck-SiC structure contains four squares and five octagons arranged as shown in Fig. 2(a), with Si-C bond lengths varying from  $1.716 - 1.876 \text{ \AA}$ . As compared to the initial structure (Fig. 1(a)), after optimization, we observe only small changes in bond lengths and angles. The final bond angles  $\angle\text{C-Si-C}$  ( $\angle\text{Si-C-Si}$ ) of the tetragon and octagon rings are in the ranges  $91^\circ - 95.3^\circ$  and  $131.5^\circ - 134.5^\circ$  ( $85.4^\circ - 90.4^\circ$  and  $134.4^\circ - 138.6^\circ$ ), respectively.

The Circular-SiC comprises seven hexagons with alternative single and double bonds, as shown in Fig. 2(b). The initial Si - C bond length of Circular-SiC lies between  $1.369 - 1.425 \text{ \AA}$ , which increases to  $1.792 - 1.815 \text{ \AA}$  after optimization. Also, the Si - H and C - H bond length changes from  $1.01 \text{ \AA}$  to  $1.493 \text{ \AA}$  and  $1.01 \text{ \AA}$  to  $1.094 \text{ \AA}$ , respectively. The bond angles  $\angle\text{Si-C-Si}$ , and  $\angle\text{C-Si-C}$  of Circular-SiC lie between  $118.4^\circ - 123.2^\circ$  and  $118.8^\circ - 122.5^\circ$ , as listed in Table 2.

Next, the Tho-SiC QD is composed of six hexagons, three squares, and two octagons arranged, as shown in Fig. 2(c). Its minimum and maximum Si - C bond lengths initially are  $1.456 \text{ \AA}$ ,  $1.810 \text{ \AA}$ , while after optimization they get elongated to  $1.751 \text{ \AA}$ ,  $1.835 \text{ \AA}$ , respectively. The range of  $\angle\text{C-Si-C}$  ( $\angle\text{Si-C-Si}$ ) in tetragon, hexagon, and octagon is  $94.2^\circ - 95.1^\circ$ ,  $115.1^\circ - 125.4^\circ$ , and  $122.8^\circ - 142.3^\circ$  ( $84.9^\circ - 85.8^\circ$ ,  $112^\circ - 122^\circ$ , and  $122.2^\circ - 152.9^\circ$ ), respectively.

As seen in Fig. 2(d), the Pho-SiC QD is made up of eight pentagons, 13 hexagons, and two octagons. The initial minimum and maximum Si - C bond lengths in this case are  $1.752 \text{ \AA}$  and  $1.880 \text{ \AA}$ , respectively. The Pho structure also contains Si - Si bonds whose initial bond length varies in between  $2.237 - 2.281 \text{ \AA}$ . The corresponding optimized bond lengths of Si - C and Si - Si lie between  $1.417 - 2.271 \text{ \AA}$  and  $2.237 - 2.268 \text{ \AA}$ . Thus, as compared to the initial values, we observe some bond compression in this case. The optimized bond angles  $\angle\text{C-Si-C}$  ( $\angle\text{Si-C-Si}$ ) of the pentagon, hexagon, and octagon vary between  $104.8^\circ - 109.3^\circ$  ( $101^\circ - 104.7^\circ$ ),  $115.7^\circ - 121.2^\circ$  ( $107.5^\circ - 122.5^\circ$ ), and  $131.5^\circ - 135.6^\circ$  ( $131.3^\circ - 140.2^\circ$ ), respectively.

Figure 2(e) shows that T1-SiC QD has two types of hexagons with four C atoms and two Si atoms in the first type, and two Si atoms and four C atoms in the second type. All the initial Si - C, C - C and Si - Si bonds were taken to be of same lengths  $1.756 \text{ \AA}$ ,  $1.401 \text{ \AA}$ , and  $2.219 \text{ \AA}$ , respectively. After optimization, however, we note that C - C, C - Si and Si - Si bond lengths vary between  $1.406 - 1.463 \text{ \AA}$ ,  $1.781 \text{ \AA} - 1.831 \text{ \AA}$ , and  $2.267 - 2.268 \text{ \AA}$ , respectively. The optimized  $\angle\text{C-Si-C}$  ( $\angle\text{Si-C-Si}$ ) bond angles vary in the range  $116.4^\circ - 119.9^\circ$  ( $118.6^\circ - 119.3^\circ$ ), while for all the other bond angles the range is provided in Table 2.

Finally, the Triangular-SiC QD is made up of six hexagons arranged in a triangular fashion with zigzag edges as shown in Fig. 2(f.) This is a graphitic structure, with the optimized C-Si bond lengths in the range  $1.770 \text{ \AA} - 1.821 \text{ \AA}$ , and the  $\angle\text{C-Si-C}$  ( $\angle\text{Si-C-Si}$ ) bond angles in the range  $119.6^\circ - 123.3^\circ$  ( $118.1^\circ - 122.7^\circ$ ).

In general, the Si-H and C-H bond lengths show less variation for all the QDs whose values are recorded in Table 1. In summary, the order of Si-C maximum bond length is Pho-SiC > Haeck-SiC > Tho-SiC > T1-SiC > Triangular-SiC > Circular-SiC. The alteration in the bond lengths and bond angles of the considered structures suggests distortions in the shapes of tetragons, hexagons, and octagons, as compared to their ideal structures.

Table 1: Size, formation energies, and bond lengths of (a) Haeck-SiC (b) Circular-SiC (c) Tho-SiC (d) Pho-SiC (e) T1-SiC (f) Triangular-SiC

Structure	Size of QD (nm)	$E_b$ (eV)	C – C(Å)	Si – Si (Å)	Si – H (Å)	C – H (Å)	Si – C (Å)
			Min.-Max.	Min.-Max.	Min.-Max.	Min.-Max.	Min.-Max.
Haeck	1.652	-5.123	-	2.457	1.488-1.493	1.093-1.099	1.716-1.876
Circular	1.195	-5.281	-	-	1.493	1.094	1.792-1.815
Tho	1.857	-5.306	-	2.463-2.477	1.491-1.493	1.092-1.094	1.751-1.835
Pho	2.278	-5.684	1.417-1.463	2.240-2.271	1.486-1.493	1.090-1.093	1.752-1.880
T1	1.382	-5.357	1.406-1.463	2.267-2.268	1.484-1.485	1.097	1.781-1.831
Triangular	1.2	-4.999	-	-	1.489-1.490	1.094	1.770-1.821

Table 2: The minimum, maximum, and average values of Bond angles

Structure	Shape	$\angle C - Si - C(^{\circ})$		$\angle Si - C - Si (^{\circ})$		$\angle C - Si - Si (^{\circ})$		$\angle C - C - Si (^{\circ})$		$\angle C - C - C (^{\circ})$	
		Min.-Max.	Average	Min.-Max.	Average	Min.-Max.	Average	Min.-Max.	Average	Min.-Max.	Average
		Haeck	Tetragon	91-95.3	93.2	85.4-90.4	87.1	-	-	-	-
	Octagon	131.5-134.5	132.8	134.4-138.6	136.1	-	-	-	-	-	-
Circular	Hexagon	118.8-122.5	120.6	118.4-123.2	120.1	-	-	-	-	-	-
Tho	Tetragon	94.2-95.1	94.8	84.9-85.8	85.2	-	-	-	-	-	-
	Hexagon	115.1-125.4	121.3	112-122	118.1	-	-	-	-	-	-
	Octagon	122.8-142.3	132.4	122.2-152.9	137.6	-	-	-	-	-	-
Pho	Pentagon	104.8-109.3	106.8	101-104.7	102.8	-	-	110.2-113.8	111.8	-	-
	Hexagon	115.7-121.2	119	107.5-122.5	115.7	112.3-128.8	120	122.9-126	124.1	123.7-124.9	124.2
	Octagon	131.5-135.6	133.9	131.3-140.2	136.0	-	-	-	-	-	-
T1	Hexagon	116.4-119.9	117.7	118.6-119.3	119	120.6-123.0	121.5	120.2-122.8	121.1	-	-
Triangular	Hexagon	119.6-123.3	120.9	118.1-122.7	120	-	-	-	-	-	-

### 3.2. Binding Energies

To analyze the energetic stability of the SiC QDs, the binding energy per atom is calculated using the formula

$$E_b = \frac{1}{N_{atom}}(E_{total} - n_H E_H - n_C E_C - n_{Si} E_{Si}),$$

where  $n_H$ ,  $n_C$ ,  $n_{Si}$ ,  $N_{atom}$  respectively represent the numbers of H, C, Si atoms in the SiC-QD, while the total number of atoms  $N_{atom} = n_H + n_C + n_{Si}$ . The calculated energy of the SiC QD is represented by  $E_{total}$  here, whereas  $E_H$ ,  $E_C$ ,  $E_N$  are the energies of the respective isolated H, C, and Si atoms. The calculated binding energies for all the SiC QDs are presented in Table 1 and are negative indicating that they can be synthesized in an energetically favourable way. The calculated binding energies per atom are close to each other, but their values in descending order inclusive of the sign follow Triangular-SiC > Haeck-SiC > Circular-SiC > Tho-SiC > T1-SiC > Pho-SiC. As the Pho-SiC possesses the most negative binding energy, its formation is most favourable compared to all other QDs.



Table 3: Our calculated H-L gaps of various SiC QDs compared to the band gaps of their 2D-periodic counterparts. Above  $\alpha$  denotes spin up, while  $\beta$  denotes spin down in the UHF calculations. Because of the UHF open-shell triplet ground state, Triangular-SiC has different H-L gaps for up- and down-spin electrons.

QD Structure	$E_{HL}$ (eV)	periodic monolayer	$E_{HL}$ (eV)
Haeck-SiC	2.42	T-SiC	2.24/3.07[58]
Circular-SiC	3.71	g-SiC	2.56/3.48[58]
Tho-SiC	3.01	Tho-SiC	1.43/2.16[58]
Pho-SiC	0.66	Pho-SiC	Metallic[58]
T1-SiC	0.93	T1-SiC	0.00[58]
Triangular-SiC	1.34 ( $\alpha$ )/4.09( $\beta$ )	g-SiC	2.56/3.48[58]

### 3.3. Electronic Structure

*3.3.1. Nature of Molecular Orbitals* For analyzing the electronic structure and optical properties of SiC QDs, it is important to understand the nature of their frontier molecular orbitals (MOs), in general, and HOMO (Highest Occupied Molecular Orbital) and LUMO (Lowest Unoccupied Molecular Orbital) and their energies, in particular. [88] Because the final optimized geometries of all the SiC QDs are planar (see Fig. 2), we expect the frontier MOs to have the delocalized  $\pi$ -electron character. In table 3 and Fig. 3 we present the plots of HOMO (H) and LUMO (L) orbitals of each SiC QD from which it is obvious that they are of  $\pi$ -type, delocalized on the Si and C atoms of the QDs, but with a negligible presence on the passivating hydrogen atoms. In Table 4 we list the  $\pi/\pi^*$  orbitals closest to the Fermi energy, from which it is obvious that it is not just the H/L orbitals which have the  $\pi$  character, rather a large number of occupied and unoccupied frontier orbitals have that character. This is similar to the case of planar aromatic hydrocarbons, therefore, we expect the electronic properties and the low-lying excited states of these SiC QDs to be determined by their  $\pi$ -electron dynamics.

Furthermore, the  $H$  and  $L$  energy values characterize the electrophilic and nucleophilic behaviour of the molecules[89, 90]. In Table 3 we compare our calculated H-L gaps of the SiC QDs, to the band gaps of their periodic monolayer counterparts computed using the VASP code[91, 92, 93, 94], we conclude that the gaps increase from 2D to 0D, in accordance with the quantum confinement effect. For the calculation of the band gaps listed in the last column of Table 3, two functionals GGA-PBE and HSE06 (data written as PBE/HSE06 in column IV) were utilized by Long et al. for 2D SiC siligraphene structures[58].

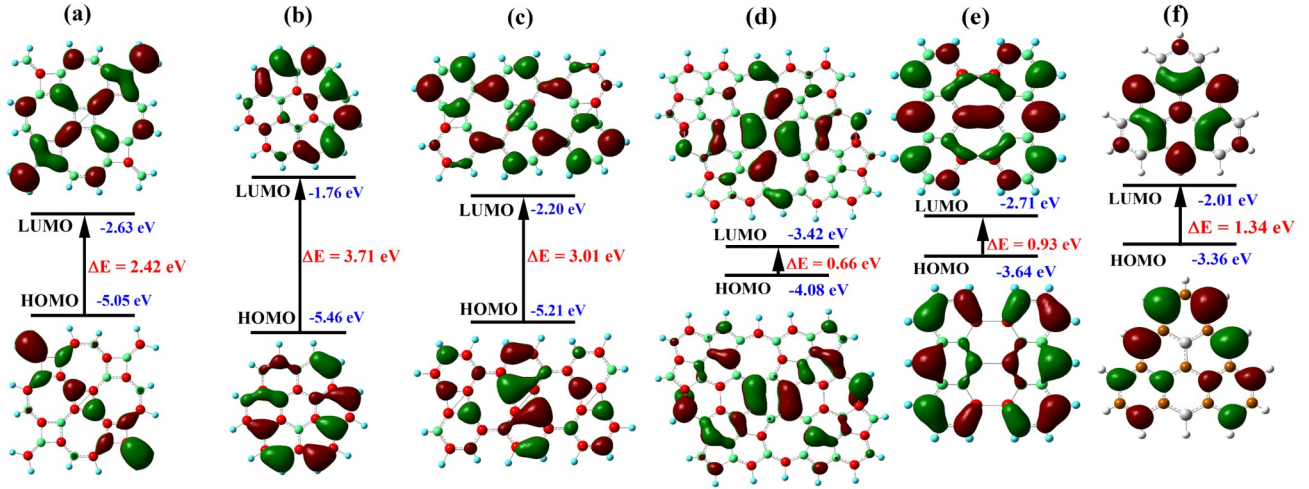


Figure 3: Plots of HOMO (H) and LUMO (L) orbitals of (a) Haec-SiC (b) Circular-SiC (c) Tho-SiC (d) Pho-SiC (e) T1-SiC (f) Triangular-SiC. The H-L gap of each QD is also indicated.

Table 4: Frontier molecular orbitals with  $\pi$  and  $\pi^*$  character of the considered SiC QDs. Our notation implies, for example, that for Tho-SiC all the orbitals starting from  $H - 10$  to  $H$  and  $L$  to  $L + 9$  have  $\pi$  and  $\pi^*$  characters, respectively.

Structure	$\pi$ orbital	$\pi^*$ orbital
Haec-SiC	$H - 10 : H$	$L : L + 6$
Circular-SiC	$H - 8 : H$	$L : L + 6$
Tho-SiC	$H - 10 : H$	$L : L + 9$
Pho-SiC	$H - 14 : H$	$L : L + 11$
T1-SiC	$H - 5 : H$	$L : L + 5$
Triangular-SiC	$H - 8 : H$	$L : L + 5$

**3.3.2. Mulliken Charge Analysis** The Mulliken charge varies with the atomic arrangement in the molecule[95], therefore, it provides useful information regarding the structural dependence of the charge distribution in a molecule, and, thus, on the nature of the chemical bonding in the system.[96] Although both Si and C are group IV elements, because of their different electron affinities and ionization potentials, we expect the SiC structures to exhibit polar covalent bonds, instead of pure covalent bonds displayed in pure Si or C based systems. To verify that, we have performed the Mulliken charge analysis of these SiC QDs and divided it into two parts: a) Structural comparison, and b) atomic site comparison (electrophilic or nucleophilic) within a given QD. The charge on each SiC QD is arranged such that the net charge on the molecule is zero.

In all the QDs, Si atoms exhibit inhomogeneous positive charges, whereas C atoms exhibit negative charges. This behaviour can be explained based on the electronegativity values; C being more electronegative than Si and H exhibits negative charges, whereas Si and H atoms attached to C exhibit positive charges. In the Si-H bond, Si is more electropositive, so H attached to Si attains a negative charge. The total charge gained by the Si ( $T_{Si}$ ) and lost

Table 5: The maximum charge on a Si atom, the maximum charge on a C atom, and the total Mulliken charges carried by all the C atoms ( $T_C$ ), Si atoms ( $T_{Si}$ ), and H atoms ( $T_H$ ) for each SiC QD considered in this work.

	Maximum Charge on Si	Maximum Charge on C	$T_C$	$T_{Si}$	$T_H$
Haeck	0.369	-0.333	-4.316	4.237	0.079
Circular	0.407	-0.354	-3.724	3.956	-0.232
Tho	0.397	-0.366	-5.703	6.003	-0.301
Pho	0.399	-0.359	-7.576	7.953	-0.377
T1	0.266	-0.235	-2.579	2.79	-0.212
Triangular	0.438	-0.369	-3.055	3.411	-0.356

by the C ( $T_C$ ) for all the SiC QDs is presented in Table 5. The overall zero charge in a given QD can be confirmed by adding the total charges of H ( $T_H$ ) with  $T_{Si}$  and  $T_C$ . The maximum positive and negative charges exhibited by the SiC QDs, also presented in Table 5, help in identifying the most electrophilic and nucleophilic sites.

*3.3.3. Global Reactivity Descriptors* The values of other global reactivity descriptors that depend on the frontier orbital energies, namely, ionization potential ( $IP$ ), electron affinity ( $EA$ ), chemical potential ( $\mu$ ), chemical hardness ( $\eta$ ), electrophilicity index ( $\omega$ ), and chemical softness ( $S$ ) [97, 98, 99] are presented in Table 6. Based on its largest H-L gap  $E_{HL} = 3.71$  eV (see Fig. 3), we predict the circular-SiC QD to possess high kinetic stability and low chemical reactivity [100]. Its lowest energy value (-5.46 eV) of  $H$  and high energy value (-1.76 eV) of  $L$  as compared to other structures, do not favour charge transfer. Based on the H-L gap criterion, the QDs can be arranged in the descending order of kinetic stability as Circular-SiC > Tho-SiC > Haeck-SiC > Triangular-SiC( $\alpha$ ) > T1-SiC > Pho-SiC. The tendency to oppose the change in electron distribution is quantified by the chemical hardness  $\eta$  defined as  $(IP - EA)/2$ , while the ease in polarization is described by the chemical softness  $S$ , defined as  $S = 1/\eta$ . Accordingly, Pho-SiC is the easiest to polarize with the highest softness value of 3.03, whereas the Circular-SiC is the hardest to polarize with the least value of  $S = 0.54$ . The high chemical potential  $\mu = -(E_H + E_L)/2$  facilitates the charge transfer that leads to high molecular reactivity. The global electrophilicity index  $\omega = \mu^2/2\eta$  defines how much additional electronic charge the molecule can attain while remaining structurally stable. According to this, the maximum stabilization will be attained by Pho-SiC with a large  $\omega$  value of 21.31 after electronic charge transfer between H to L. The dipole moment ( $p$ ) is the global parameter that quantifies the net polarization in the ground states of molecules.[101]. From Table 6 it is obvious that the net ground-state dipole moment for the SiC QDs is very small, i.e., of the order of  $10^{-3}$ , or smaller.

#### 3.4. Raman Spectra

Our vibrational frequency analysis calculations for the SiC-QDs predicted all the frequencies to be real, indicating that the structures considered in this work are dynamically stable. Therefore, we calculated their Raman spectra presented in Fig. 4 and discussed next in detail.

The Haeck-SiC QD has 48 atoms, i.e., it has  $(3 \times 48) - 6 = 148$  vibrational modes. The low-frequency region,

Table 6: Calculated global reactivity parameters for Haeck-SiC, Circular-SiC, Tho-SiC, Pho-SiC, T1-SiC, and Triangular-SiC QDs.

Structure	$E_H$ (eV)	$E_L$ (eV)	$E_{HL}$ (eV)	$IP$ (eV)	$EA$ (eV)	$\mu$ (eV)	$\eta$ (eV)	$\omega$ (eV)	$S$ (eV $^{-1}$ )	$p$ (Debye)
Haeck-SiC	-5.05	-2.63	2.42	5.05	2.63	-3.84	1.21	6.09	0.83	0.001
Circular-SiC	-5.46	-1.76	3.71	5.46	1.76	-3.61	1.85	3.51	0.54	0.001
Tho-SiC	-5.21	-2.2	3.01	5.21	2.2	-3.71	1.5	4.56	0.66	0.006
Pho-SiC	-4.08	-3.42	0.66	4.08	3.42	-3.75	0.33	21.31	3.03	0.001
T1-SiC	-3.64	-2.71	0.93	3.64	2.71	-3.17	0.47	10.84	2.15	0.0001
Triangular-SiC	-3.36	-2.01	1.34	3.36	2.01	-2.69	0.67	5.37	1.49	0.001

0–1010  $cm^{-1}$  corresponds to Si – C, C – H, and Si – H in-plane and out-of-plane bending modes with the strongest intensity at 1004.41  $cm^{-1}$  due to CH<sub>2</sub> symmetric bending along with attached Si – C double bond stretching in the  $y$  direction. The second 1010 – 1300  $cm^{-1}$  frequency region contains in-plane Si – C stretching, C – H, and Si – C bending modes. The highest intensity in this region is attributed to the single bond Si – C stretching along the  $x$ -axis coupled with in-plane Si – C and C – H bending modes at 1200.33  $cm^{-1}$ . The two frequency modes that occur above 1300  $cm^{-1}$  are attributed to scissoring of CH<sub>2</sub> groups. The 2200 – 2251  $cm^{-1}$  frequency region belongs to Si – H stretching with the highest intensity mode observed at 2217  $cm^{-1}$ . The C – H stretching modes lie in the 3100 – 3250  $cm^{-1}$  frequency region with the highest frequency occurring at 3128.57  $cm^{-1}$  attributed to C – H stretching attached to the octagon.

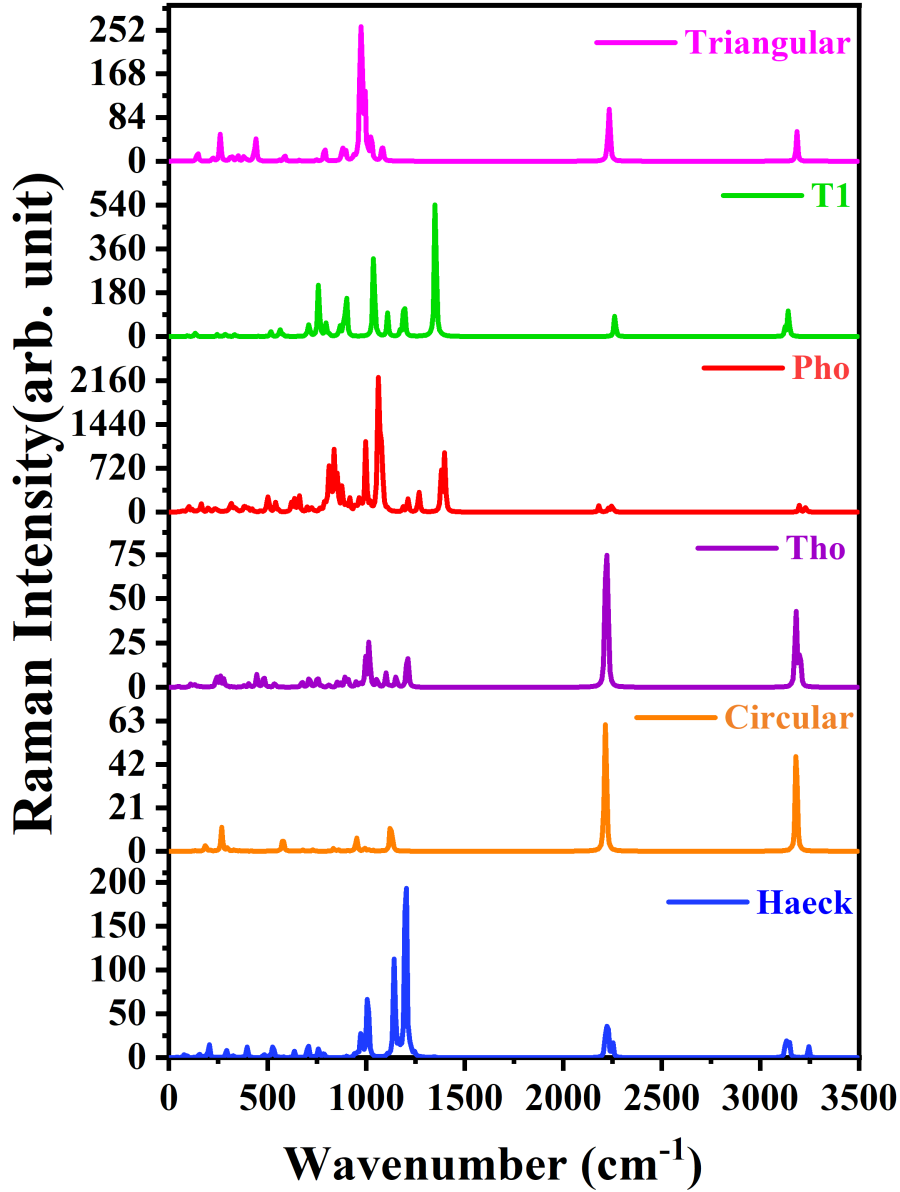


Figure 4: Calculated Raman spectra of (a) Haeck-SiC, (b) Circular-SiC, (c) Tho-SiC, (d) Pho-SiC, (e) T1-SiC, and (f) Triangular-SiC, computed using the B3LYP functional in the frequency range 0-3500  $\text{cm}^{-1}$ .

There are 36 atoms in the Circular-SiC QD leading to  $(3 \times 36) - 6 = 102$  vibrational modes. In the calculated spectrum (Fig. 4(b)) we identify three frequency regions categorized as I ( $0 - 1150 \text{ cm}^{-1}$ ) which is a broad region with several peaks, and narrow regions II ( $2200 - 2220 \text{ cm}^{-1}$ ) and III ( $3180 - 3182 \text{ cm}^{-1}$ ) with one high-intensity peak each. Starting the discussion for the region I, we note that the circular SiC lies in the  $xy$  plane, where the bending modes along positive and negative  $z$ -direction have been observed in the region  $0 - 150 \text{ cm}^{-1}$ . The out-of-plane Si-H, C-H deformations mostly occur in  $0-670 \text{ cm}^{-1}$ , and their in-plane bending vibrations are in the  $670-950 \text{ cm}^{-1}$  range. In the region,  $150-500 \text{ cm}^{-1}$ , both in-plane and out-of-plane deformations of Si - C, C-H, and Si-H

bonds have been observed. The frequency region  $500 - 950 \text{ cm}^{-1}$  is attributed to the Si-H and C-H bending modes along with three Si - C bending modes in between. The out-of-plane deformations of Si-H and C-H occur in the ranges  $0 - 530 \text{ cm}^{-1}$  and  $640 - 670 \text{ cm}^{-1}$ , while in the intermediate region the in-plane Si - C, C-H, Si-H bending modes are also observed at  $558.04 \text{ cm}^{-1}$ ,  $558.22 \text{ cm}^{-1}$ , and  $577.47 \text{ cm}^{-1}$ , respectively. The in-plane C-H and Si-H bending modes occur in the region  $670 - 950 \text{ cm}^{-1}$ . In the frequency  $950 - 1150 \text{ cm}^{-1}$  region, both stretching and bending modes have been observed in the  $xy$  plane, along with the C-H and Si-H bending modes. The medium frequency region II corresponds to Si - C stretching modes with the highest frequency of the entire spectrum at  $2220 \text{ cm}^{-1}$ . Region III is also a high-intensity region representing the C - H bond stretching having six normal modes.

Next, we discuss Tho-SiC QD with 52 atoms, and a total  $(3 \times 52) - 6 = 150$  modes. We note that the Raman spectrum of this QD is quite similar to that of the circular-SiC QD in that both have a broad lower energy region containing low-intensity peaks, followed by a couple of sharp high-intensity peaks at higher energies. The first frequency region varies from  $0 - 980 \text{ cm}^{-1}$  that contains in-plane and out-of-plane Si - C, C-H, and Si-H bending deformations. Here, the region from  $0 - 480 \text{ cm}^{-1}$  is dominated by Si-C in and out of plane deformations, whereas the region  $480 - 980 \text{ cm}^{-1}$  has major contributions from C-H and Si-H bending modes. The coupling of in-plane Si-C stretching and bending modes occurs in the  $980 - 1210 \text{ cm}^{-1}$  frequency region. The higher intensity peak at  $1014.48 \text{ cm}^{-1}$  belongs to Si-H, C-H bending modes along with the Si-C stretching and bending modes. The stretching modes of Si-H in this case begins from  $2200 \text{ cm}^{-1}$  with a total of eight modes and end at  $2227.22 \text{ cm}^{-1}$ . The C-H bond stretching with 8 frequency modes lies in between  $3170 - 3200 \text{ cm}^{-1}$ . The highest peak corresponds to the Si-H bond stretching at  $2219.78 \text{ cm}^{-1}$ , and the second highest peak due to the C-H bond stretching is located at  $3180.95 \text{ cm}^{-1}$ .

In the case of Pho-SiC QDs, there is a total of 80 atoms leading to  $(3 \times 80) - 6 = 234$  vibrational modes, while two additional bonds, C - C and Si - Si, are present in this QD as compared to other considered QDs. Most of the Raman intensity in this QD is confined in the energy region below  $1500 \text{ cm}^{-1}$ , while the higher energy region has a few very feeble peaks. For the frequency region  $0 - 620 \text{ cm}^{-1}$ , the bending in and out of plane deformations are observed for each bond of QD. In between  $620-700 \text{ cm}^{-1}$ , the Si-Si stretching modes are observed along with Si - C, C-H and Si-H bending modes, while Si-C stretching modes lie in the range  $815 - 1112 \text{ cm}^{-1}$ . The C-C bending and C-C stretching modes range from  $1150 - 1200 \text{ cm}^{-1}$  and  $1350 - 1400 \text{ cm}^{-1}$ , respectively, coupled with other bond bending deformations. Very weak Si-H intensity has been observed in the range  $2180.49 - 2254.05 \text{ cm}^{-1}$ , with 12 Si-H stretching modes having the highest peak at  $2180.88 \text{ cm}^{-1}$ . The C-H stretching modes lie in the  $3196 - 3250 \text{ cm}^{-1}$  frequency region with eight stretching bonds and the maximum intensity mode at  $3196.73 \text{ cm}^{-1}$ . For the fifth considered structure T1-SiC QD, there are 42 atoms with a total of  $(3 \times 42) - 6 = 120$  vibrational modes. The  $0 - 550 \text{ cm}^{-1}$  frequency region corresponds to in-plane ( $xy$  plane) and out-of-plane (i.e., along +ve and -ve  $z$ -axis) deformations of C - C, Si - Si, Si - C, Si - H, and C - H bonds. The frequency region  $550 - 600 \text{ cm}^{-1}$

contains Si – Si bond stretching coupled with C – C and C – Si bending modes. The region  $600 - 850 \text{ cm}^{-1}$  dominates with Si – H and C – H bending modes and also contains a few Si – C, C – C, and Si – Si bending deformations. The C – Si stretching modes lie in the frequency region  $850 - 1100 \text{ cm}^{-1}$  along with the rest of the bonds bending deformations. The region  $1150 - 1400 \text{ cm}^{-1}$  contains C-C stretching modes coupled with Si–H, C–H, and Si–C bending modes. The highest peak in T1 QD belongs to this region at  $1345.06 \text{ cm}^{-1}$  and corresponds to the coupled C – C stretching and bending modes. The 6 Si – H stretching modes with low intensity lie between  $2250 \text{ cm}^{-1} - 2270 \text{ cm}^{-1}$  with maximum intensity at  $2259.20 \text{ cm}^{-1}$ . The frequency region for the C – H stretching modes ranges from  $3120 \text{ cm}^{-1} - 3150 \text{ cm}^{-1}$  with a total of eight stretching modes, and the maximum intensity at  $3141.51 \text{ cm}^{-1}$ .

Lastly, in this work, we have presented the Raman spectra of Triangular-SiC QD with a total of 34 atoms, and  $(3 \times 34) - 6 = 96$  vibrational modes. The first frequency starts with a low intensity region that varies between  $0 - 600 \text{ cm}^{-1}$  containing in and out of plane bending modes for the whole QD. The region  $600 - 900 \text{ cm}^{-1}$  corresponds to the Si–H and C–H bending modes. The frequency region  $900 \text{ cm}^{-1} - 1050 \text{ cm}^{-1}$  is attributed to the Si – C stretching modes, with the rest of the bonds undergoing bending deformations. Here, the frequency region  $2217.36 - 2235.29 \text{ cm}^{-1}$  corresponds to the Si – H stretching modes with the highest frequency at  $2232.53 \text{ cm}^{-1}$ , with a total of nine Si – H stretching modes. All three C–H stretching modes have the same intensity and lie in the range  $3183.72 - 3183.91 \text{ cm}^{-1}$  corresponding to the stretching of one C-H bond at a time.

We believe that our detailed computed Raman spectra of the considered SiC-QDs can be used to interpret future Raman experiments on these QDs, and help with their structural characterization.

### 3.5. Optical Absorption Spectra

In order to compute the linear optical absorption spectra, we performed the time-dependent-DFT (TDDFT) calculations on each QD using the B3LYP hybrid functional and cc-pVDZ basis set, as was done for the ground-state calculations. Absorption spectra were computed using the sum-over-states (SOS) approach, and for this purpose 20 excited states were included for each QD implying that the computed spectra must be quite accurate in the UV-Vis region of the spectrum. In Fig. 5 we present the calculated TDDFT spectra of all the SiC-QDs, while in Table 7 we present the information such as energetic locations, wavelengths, oscillator strength (OS), dominant configurations of their first computed excited states. From Table 7 it is obvious that for two SiC-QDs, the first excited states are dipole forbidden, while for several others they are weakly allowed. Only for T1-SiC, the first peak is strongly allowed with a significant OS. In the descending order of the first excited state energies ( $E_1$ ), the SiC-QDs can be arranged as Circular-SiC > Tho-SiC > Haeck-SiC > T1-SiC > Pho-SiC. The Triangular-SiC QD is the only QD which exhibits a triplet ground state, as a result of which all its optically excited states also have triplet multiplicity. We also note that for all the QDs,  $E_1 < E_{HL}$ , because of the inclusion of the electron-hole interaction effects in the TDDFT approach.

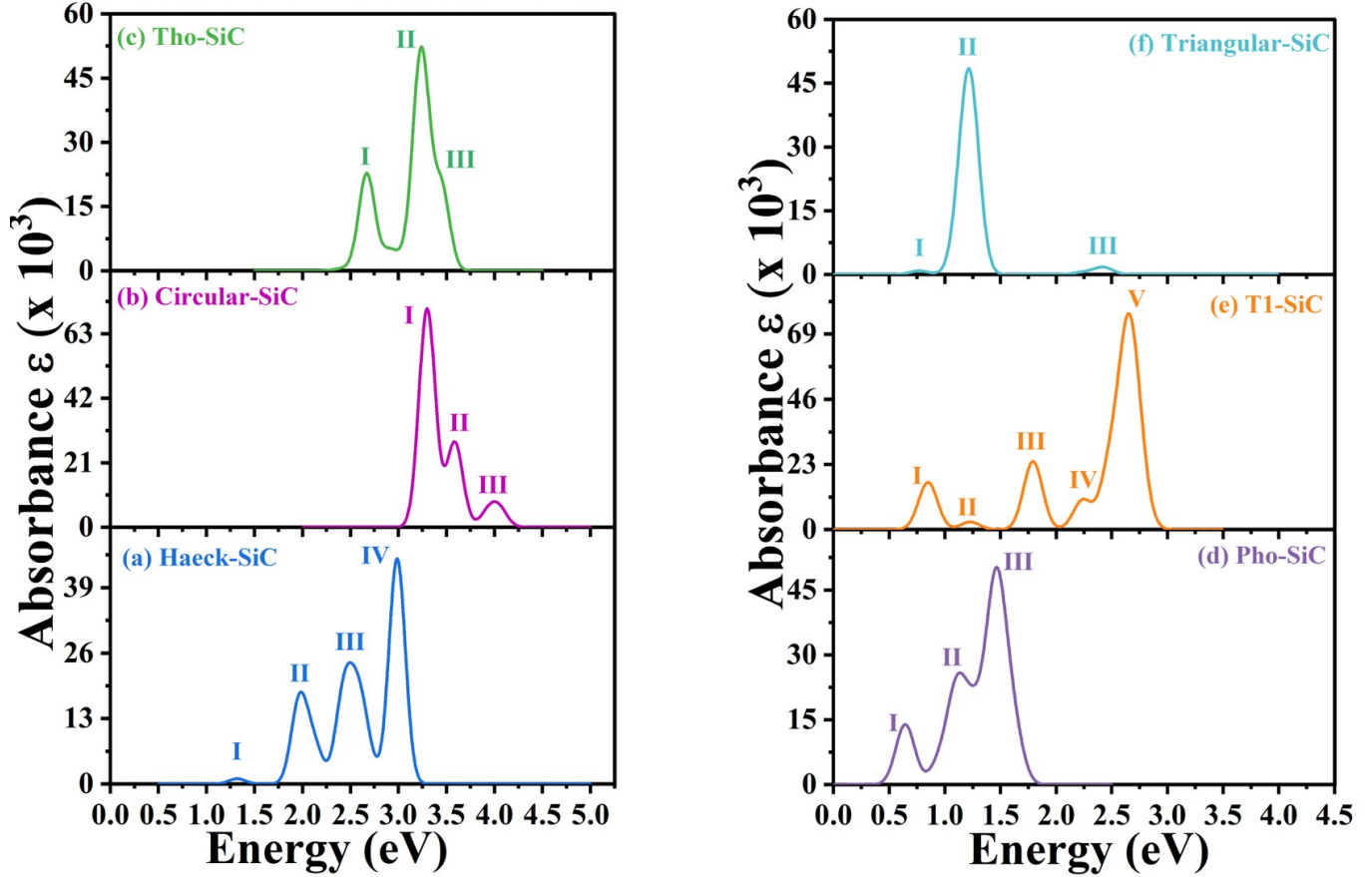


Figure 5: Linear optical absorption spectra for (a) Haeck-SiC, (b) Circular-SiC, (c) Tho-SiC, (d) Pho-SiC, (e) T1-SiC, and (f) Triangular-SiC, computed at the TDDFT-B3LYP level of theory. For plotting the spectra, a uniform line width of 0.1 eV was assumed.

From the plotted absorption spectra (Fig. 5) it is obvious that all the SiC-QDs have more than one peak. Therefore, we present detailed information about the spectra of the individual QDs in Tables 8-13 and discuss them next. The numbers in the parenthesis in the last column in Tables 7-13 represent the coefficients of those configurations in the many-body wave functions of various excited states.

Table 7: The first excited state energy ( $E_1$ ), corresponding wavelength,  $H - L$  gap ( $E_{HL}$ ), oscillator strength (OS), and the dominant configuration of the TDDFT wave function of the SiC QDs. In the last column, we list the excitations contributing to various excited states, with their coefficients in the parenthesis.

Structure	$E_1$ (eV)	$\lambda$ (nm)	$E_{HL}$ (eV)	OS	Dominant Configurations
Haeck-SiC	1.271	975.54	2.42	0	$ H \rightarrow L\rangle$ (0.7042)
Circular-SiC	2.913	425.63	3.71	0	$ H - 1 \rightarrow L\rangle$ and c.c. (0.4283)
Tho-SiC	2.416	513.16	3.01	0.0039	$ H \rightarrow L\rangle$ (0.6812)
Pho-SiC	0.191	6495.68	0.66	0.006	$ H \rightarrow L\rangle$ (0.7232)
T1-SiC	0.848	1462.50	0.93	0.1235	$ H \rightarrow L\rangle$ (0.7217)
Triangular-SiC	0.771	1608.21	1.34	0.0031	$ L(\alpha) \rightarrow L(\alpha + 1)\rangle$ (0.9572)

3.5.1. *Haeck-SiC* The first transition in Haeck-SiC corresponds to a dipole-forbidden dark state whose wave function is dominated by the excitation  $H \rightarrow L$ . As shown in Fig. 5(a), the first observable peak is feeble and



located at 1.31 eV with the main contribution from the excitation  $H \rightarrow L + 1$  (See Table 8). The next two peaks (II and III) have considerable intensity with oscillator strengths of 0.1199 and 0.1084, respectively. The transitions  $H - 2 \rightarrow L + 1$  and  $H - 5 \rightarrow L$  lead to a second peak corresponding to the excitation energy of 1.97 eV. The third peak with transition energy 2.419 eV is also a linear combination of two state transitions  $H \rightarrow L + 3$  and  $H - 4 \rightarrow L + 1$ . The fourth peak, which has the maximum intensity, is due to an excited state located at 2.99 eV, dominated by the transition  $H - 3 \rightarrow L + 2$ .

Table 8: The essential information about the excited states contributing to various peaks in the linear optical absorption spectrum of the Haeck-SiC QD (see Fig. 5(a)). In the wave function column, we list the excitations contributing to various excited states, with their coefficients in the parenthesis.

Peak	Energy(eV)	OS	Wave function
I	1.311	0.0067	$ H \rightarrow L + 1\rangle(0.6987)$
II	1.966	0.1199	$ H - 2 \rightarrow L + 1\rangle(0.6818)$ $ H - 5 \rightarrow L\rangle(0.1649)$
III	2.419	0.1084	$ H \rightarrow L + 3\rangle(0.6177)$ $ H - 4 \rightarrow L + 1\rangle(0.1388)$
IV	2.986	0.3320	$ H - 3 \rightarrow L + 2\rangle(0.6193)$

*3.5.2. Circular-SiC* In Circular-SiC, which is the SiC counterpart of coronene, the lowest excited state  $E_1$  does not play a role in the absorption spectrum because it is dipole forbidden (see Table 7). Furthermore, the second excited state whose wave function is dominated by the excitation  $H \rightarrow L$  is also dipole forbidden. The first peak (I) is the most intense peak of the spectrum which derives dominant contributions from  $H \rightarrow L + 1$  and its electron-hole conjugate excitation  $H - 1 \rightarrow L$ , referred to as “complex conjugate”, and denoted as “c.c.”, for the sake of brevity (see table 9). The second peak at 3.585 eV also has a large OS with the dominant transitions as  $H - 1 \rightarrow L + 3$  and  $H \rightarrow L + 2$ . The third peak has a comparatively smaller OS and is dominated by transitions  $H - 4 \rightarrow L$  and  $H - 5 \rightarrow L + 1$ .

Table 9: The essential information about the excited states contributing to various peaks in the linear optical absorption spectrum of the circular-SiC QD (see Fig. 5(b)). In the wave function column, we list the excitations contributing to various excited states, with their coefficients in the parenthesis.

Peak	Energy(eV)	OS	Wave function
I	3.298	0.2635	$ H \rightarrow L + 1\rangle$ and c.c.(0.3469)
II	3.585	0.1021	$ H - 1 \rightarrow L + 3\rangle(0.3852)$ $ H \rightarrow L + 2\rangle(-0.3839)$
III	4.043	0.022	$ H - 4 \rightarrow L\rangle(0.5781)$ $ H - 5 \rightarrow L + 1\rangle(0.3090)$

*3.5.3. Tho-SiC* In Tho-SiC, the optical gap corresponds to the  $E_1$  state whose wave function is dominated by the  $H \rightarrow L$  excitation and gives rise to a feeble peak in the spectrum located at 2.416 eV which is not shown in

Fig. 5(c)). The wavelength corresponding to  $E_1$  is 513.2 nm, which clearly lies in the visible region (Table 7). In Fig. 5(c) and Table 10, the first peak is observed at 2.669 eV, also in the visible region, which is dominated by  $H - 2 \rightarrow L$  transition. The wave function of the most intense peak (II) located at 3.241 eV has major contributions from  $H - 4 \rightarrow L$  and  $H - 3 \rightarrow L + 2$  transitions. The last peak appears as a shoulder of peak II, and its wave function is dominated by the excitation  $H - 1 \rightarrow L + 4$ .

Table 10: The essential information about the excited states contributing to various peaks in the linear optical absorption spectrum of Tho-SiC QD (see Fig. 5(c)). In the wave function column, we list the excitations contributing to various excited states, with their coefficients in the parenthesis.

Peak	Energy(eV)	OS	Wave function
I	2.669	0.1668	$ H - 2 \rightarrow L\rangle$ (0.6203)
II	3.241	0.3424	$ H - 4 \rightarrow L\rangle$ (0.6203) $ H - 3 \rightarrow L + 2\rangle$ (0.2481)
III	3.447	0.1423	$ H - 1 \rightarrow L + 4\rangle$ (0.6305)

*3.5.4. Pho-SiC* The optical gap of Pho-SiC is quite small at 0.191 eV, corresponding to the  $E_1$  state with a small OS (see Table 7) whose wave function is dominated by the  $H \rightarrow L$  excitation. As far as its optical absorption spectrum presented in Fig. 5(d) is concerned, the first peak at 0.644 eV involves  $H - 2 \rightarrow L$  transition for the dominant contribution towards the wave function along with a minor contribution from  $H \rightarrow L$  excited state (see table 11). The second peak at 1.104 eV comprises two excitations  $H - 1 \rightarrow L + 1$  and  $H \rightarrow L + 2$  with significant contributions. The final peak is the maximum intensity peak located at 1.447 eV with the dominant contribution from the  $H \rightarrow L + 4$  excitation. We note that the optical excitation energies of this QD are much smaller as compared to others, and, could be of potential use in low-energy optoelectronics.

Table 11: The essential information about the excited states contributing to various peaks in the linear optical absorption spectrum of Pho-SiC QD (see Fig. 5(d)). In the wave function column, we list the excitations contributing to various excited states, with their coefficients in the parenthesis.

Peak	Energy(eV)	OS	Wave function
I	0.644	0.1031	$ H - 2 \rightarrow L\rangle$ (0.6621) $ H \rightarrow L\rangle$ (0.1462)
II	1.104	0.154	$ H - 1 \rightarrow L + 1\rangle$ (0.5232) $ H \rightarrow L + 2\rangle$ (0.3547)
III	1.447	0.2234	$ H \rightarrow L + 4\rangle$ (0.6379)

*3.5.5. T1-SiC* In Table 12 we present the essential information about the excited states contributing to the absorption spectrum of T1-SiC (see Fig. 5(e)). The first excited state  $E_1$  located at 0.848 eV in T1-SiC has a significant OS in the absorption spectrum and gives rise to peak I in the absorption spectrum. Given the fact that its wave function is dominated by the excitation  $H \rightarrow L$ ,  $E_1$  clearly corresponds to the optical gap of the T1-SiC QD. Thus, the optical gap of this QD (0.848 eV) is less than that of Tho-SiC (2.416 eV), but more than

that of Pho-SiC (0.191 eV). The first peak is followed by a feeble peak, i.e., peak II at 1.227 eV with the dominant contributions from  $H \rightarrow L + 2$  and  $H \rightarrow L$  excitations. The third peak (III) at 1.79 eV is the moderately intense peak composed of two excitations  $H \rightarrow L + 4$  and  $H - 1 \rightarrow L + 1$ . The fourth peak in the spectrum appears as a shoulder of peak V and is characterized by the configurations  $H - 1 \rightarrow L + 1$  and  $H - 1 \rightarrow L + 3$ . The most intense peak in the absorption spectrum (peak V) is located at 2.634 eV and is dominated by the configurations  $H - 1 \rightarrow L + 3$  and  $H - 4 \rightarrow L$ . Given the fact that similar to Pho-SiC, several peaks of T1-SiC QD are also in the low-energy region, it could be useful in infrared optics.

Table 12: The essential information about the excited states contributing to various peaks in the linear optical absorption spectrum of T1-SiC QD (see Fig. 5(e)). In the wave function column, we list the excitations contributing to various excited states, with their coefficients in the parenthesis.

Peak	Energy(eV)	OS	Wave function
I	0.848	0.1235	$ H \rightarrow L\rangle$ (0.7217)
II	1.227	0.02	$ H \rightarrow L + 2\rangle$ (0.6976) $ H \rightarrow L\rangle$ (-0.1002)
III	1.790	0.1781	$ H \rightarrow L + 4\rangle$ (0.6521) $ H - 1 \rightarrow L + 1\rangle$ (-0.2325)
IV	2.237	0.0769	$ H - 1 \rightarrow L + 1\rangle$ (0.6344) $ H - 1 \rightarrow L + 3\rangle$ (-0.219)
V	2.634	0.3652	$ H - 1 \rightarrow L + 3\rangle$ (0.6094) $ H - 4 \rightarrow L\rangle$ (0.2318)

*3.5.6. Triangular-SiC* The spin-polarized DFT calculations on this QD predict the ground state to have a triplet spin multiplicity, in agreement with the well-known property of the corresponding carbon-based triangulene. In our all-electron calculations consisting of 240 electrons, we nominally call the HOMO to be the 120th energetically ordered orbital, irrespective of whether the orbital corresponds to up-spin ( $\alpha$ ) or down-spin ( $\beta$ ). Thus the ground state has the frontier-orbital occupancy  $H^1(\alpha)L^1(\alpha)$  for the up spins, and  $(H - 1)^1(\beta)$  for the down spin. Subsequently, spin-polarized TDDFT calculations were performed, and the computed optical absorption spectrum is presented in Fig. 5(f), while the detailed information about the peaks is presented in Table 13. We note that all the configurations contributing to the excited-state wave functions are single excitations in the  $\alpha$ -spin sector, therefore, we have suppressed the spin orientation of the excitations in the table. Peak I of the spectrum is quite weak and corresponds to the first excited state  $E_1$  located at 0.771 eV, representing the optical gap whose wave function is dominated by the excitation  $L(\alpha) \rightarrow L + 1(\alpha)$ . The middle peak (II) is the most intense one located at 1.224 eV and has almost equally dominant contributions from three excitations  $L(\alpha) \rightarrow L + 2(\alpha)$ ,  $L(\alpha) \rightarrow L + 3(\alpha)$ , and  $H(\alpha) \rightarrow L + 4(\alpha)$ . The final peak is again a very feeble one with the dominant contribution from the excitation  $H(\alpha) \rightarrow L + 8(\alpha)$ .

Peak	Energy(eV)	OS	Wave function
I	0.771	0.0031	$ L \rightarrow L + 1\rangle(0.9572)$
II	1.224	0.1541	$ L \rightarrow L + 2\rangle(0.5446)$
			$ L \rightarrow L + 3\rangle(0.5062)$
			$ H \rightarrow L + 4\rangle(0.5033)$
III	2.424	0.0063	$ H \rightarrow L + 8\rangle(0.9317)$
			$ L \rightarrow L + 5\rangle(0.2063)$

Table 13: The essential information about the excited states contributing to various peaks in the linear optical absorption spectrum of Triangular-SiC QD (see Fig. 5(f)). In the wave function column, we list the excitations contributing to various excited states, with their coefficients in the parenthesis. For this QD, all the excitations are in the  $\alpha$ -spin sector.

From Table 13, we note that all the peaks lie in the range spanning the infrared to the visible region of the optical spectrum.

#### 4. Conclusions and Future Directions

In this work, we studied the structural, electronic, vibrational, and optical properties of six nanometer-sized finite fragments, i.e., quantum dots, of several recently proposed 2D monolayers of SiC. The considered QDs have different topological characteristics, with their edges passivated by hydrogen atoms. The binding energy and vibrational frequency calculations indicated that all six predicted SiC-QDs are thermodynamically and structurally stable. The computed Raman as well as optical absorption spectra contain structural fingerprints of different QDs, thus, we believe that once synthesized, these spectroscopies can be used to identify them.

The optical gaps of the considered QDs show significant variation from 0.64 eV (Pho-SiC) to 3.30 eV (Circular-SiC), indicating that our predicted SiC-QDs can be useful in devices operating from the infrared to the ultraviolet region of the optical spectrum.

On examining the TDDFT many-particle wave functions of the optically active excited states of these QDs, we found the dominant contributing configurations to have  $\pi \rightarrow \pi^*$  character, with negligible contributions from excitations involving  $\sigma/\sigma^*$  orbitals. This is similar to the case of planar aromatic hydrocarbons for which  $\sigma$ - $\pi$  separation holds good when it comes to low-lying optically excited states in the UV-Vis region. Therefore, one can obtain an effective  $\pi$ -electron Hamiltonian for planar SiC-QDs for describing their optical excitations, similar to the PPP model[102] for the aromatic hydrocarbon molecules and H-passivated graphene fragments used extensively in our group[72, 103, 73]. We plan to develop such an effective model Hamiltonian for SiC and other similar planar  $\pi$ -conjugated systems in future because it will allow us to perform more rigorous electron-correlated calculations due to a drastic reduction in the degrees of freedom achieved in making a transition from the first-principles all-electron approach to the one involving only the  $\pi$ -electrons.

Furthermore, this work was restricted only to the study of the linear optical response of these SiC-QDs. However,  $\pi$ -conjugated molecules, particularly aromatic hydrocarbons are known for their strong nonlinear optical

response (NLOR) as well. However, given their high level of symmetry, the first NLOR in aromatic molecules is typically in the third order. On the other hand, for the heteroatom  $\pi$ -conjugated structures such as SiC-QDs considered here, we expect their NLOR to be in the second order, therefore, it will be worthwhile to study processes such as second-harmonic generation in them. At present calculations along these lines are underway in our group, and the results will be presented in future publications.

### Author Information

#### Corresponding Authors

Alok Shukla: \*E-mail: shukla@phy.iitb.ac.in

#### Notes

The authors declare no competing financial interests.

### Acknowledgements

One of the authors, RJ acknowledges financial assistance from CSIR JRF.

### References

- [1] Yakimova, R.; Petoral, R.; Yazdi, G.; Vahlberg, C.; Spetz, A. L.; Uvdal, K. Surface functionalization and biomedical applications based on SiC. *Journal of Physics D: Applied Physics* **2007**, *40*, 6435.
- [2] Katoh, Y.; Snead, L. L.; Szlufarska, I.; Weber, W. J. Radiation effects in SiC for nuclear structural applications. *Current Opinion in Solid State and Materials Science* **2012**, *16*, 143–152.
- [3] Goldberg, Y.; Levinshtein, M.; Rumyantsev, S. Silicon carbide (SiC). *Properties of Advanced Semiconductor Materials: GaN, AlN, InN, BN, SiC, SiGe* **2001**, *93*.
- [4] Ledoux, M. J.; Hantzer, S.; Huu, C. P.; Guille, J.; Desaneaux, M.-P. New synthesis and uses of high-specific-surface SiC as a catalytic support that is chemically inert and has high thermal resistance. *Journal of Catalysis* **1988**, *114*, 176–185.
- [5] Kowbel, W.; Bruce, C.; Tsou, K.; Patel, K.; Withers, J.; Youngblood, G. High thermal conductivity SiC/SiC composites for fusion applications. *Journal of Nuclear Materials* **2000**, *283*, 570–573.
- [6] Xie, H.-q.; Wang, J.-c.; Xi, T.-g.; Liu, Y. Thermal conductivity of suspensions containing nanosized SiC particles. *International Journal of Thermophysics* **2002**, *23*, 571–580.
- [7] Goela, J.; Brese, N.; Burns, L.; Pickering, M. *High thermal conductivity materials*; Springer, 2006; pp 167–198.

- [8] Baliga, B. Trends in power semiconductor devices. *IEEE Transactions on Electron Devices* **1996**, *43*, 1717–1731.
- [9] Casady, J.; Johnson, R. W. Status of silicon carbide (SiC) as a wide-bandgap semiconductor for high-temperature applications: A review. *Solid-State Electronics* **1996**, *39*, 1409–1422.
- [10] Cooper, J. A.; Agarwal, A. SiC power-switching devices-the second electronics revolution? *Proceedings of the IEEE* **2002**, *90*, 956–968.
- [11] Verma, A.; Krishna, P. *Polymorphism and Polytypism in Crystals*; Wiley (New York), 1966.
- [12] Jepps, N.; Page, T. Polytypic transformations in silicon carbide. *Progress in Crystal Growth and Characterization* **1983**, *7*, 259–307.
- [13] Park, C.; Cheong, B.-H.; Lee, K.-H.; Chang, K.-J. Structural and electronic properties of cubic, 2H, 4H, and 6H SiC. *Physical Review B* **1994**, *49*, 4485.
- [14] Käckell, P.; Wenzien, B.; Bechstedt, F. Electronic properties of cubic and hexagonal SiC polytypes from ab initio calculations. *Physical Review B* **1994**, *50*, 10761.
- [15] Lee, K.-H.; Park, C.; Cheong, B.-H.; Chang, K.-J. First-principles study of the optical properties of SiC. *Solid State Communications* **1994**, *92*, 869–872.
- [16] Cobet, C.; Wilmers, K.; Wethkamp, T.; Edwards, N.; Esser, N.; Richter, W. Optical properties of SiC investigated by spectroscopic ellipsometry from 3.5 to 10 eV. *Thin Solid Films* **2000**, *364*, 111–113.
- [17] Devaty, R.; Choyke, W. Optical characterization of silicon carbide polytypes. *physica status solidi (a)* **1997**, *162*, 5–38.
- [18] Kildemo, M. Optical properties of silicon carbide polytypes below and around bandgap. *Thin Solid Films* **2004**, *455*, 187–195.
- [19] Karch, K.; Bechstedt, F.; Pavone, P.; Strauch, D. Pressure-dependent properties of SiC polytypes. *Physical Review B* **1996**, *53*, 13400.
- [20] Choyke, W.; Pensl, G. Physical properties of SiC. *Mrs Bulletin* **1997**, *22*, 25–29.
- [21] Limpijumngong, S.; Lambrecht, W. R.; Rashkeev, S. N.; Segall, B. Optical-absorption bands in the 1–3 eV range in n-type SiC polytypes. *Physical Review B* **1999**, *59*, 12890.
- [22] Kiyamaz, D.; Yagmurcukardes, M.; Tomak, A.; Sahin, H.; Senger, R. T.; Peeters, F. M.; Zareie, H. M.; Zafer, C. Controlled growth mechanism of poly (3-hexylthiophene) nanowires. *Nanotechnology* **2016**, *27*, 455604.
- [23] Hu, J.; Lu, Q.; Tang, K.; Deng, B.; Jiang, R.; Qian, Y.; Yu, W.; Zhou, G.; Liu, X.; Wu, J. Synthesis and characterization of SiC nanowires through a reduction- carburization route. *The Journal of Physical Chemistry B* **2000**, *104*, 5251–5254.

- [24] Liang, C.; Meng, G.; Zhang, L.; Wu, Y.; Cui, Z. Large-scale synthesis of  $\beta$ -SiC nanowires by using mesoporous silica embedded with Fe nanoparticles. *Chemical Physics Letters* **2000**, *329*, 323–328.
- [25] Sun, X.-H.; Li, C.-P.; Wong, W.-K.; Wong, N.-B.; Lee, C.-S.; Lee, S.-T.; Teo, B.-K. Formation of silicon carbide nanotubes and nanowires via reaction of silicon (from disproportionation of silicon monoxide) with carbon nanotubes. *Journal of the American Chemical Society* **2002**, *124*, 14464–14471.
- [26] Menon, M.; Richter, E.; Mavrandonakis, A.; Froudakis, G.; Andriotis, A. N. Structure and stability of SiC nanotubes. *Physical Review B* **2004**, *69*, 115322.
- [27] Alam, K. M.; Ray, A. K. Hybrid density functional study of armchair SiC nanotubes. *Physical Review B* **2008**, *77*, 035436.
- [28] Taguchi, T.; Igawa, N.; Yamamoto, H.; Shamoto, S.-i.; Jitsukawa, S. Preparation and characterization of single-phase SiC nanotubes and C-SiC coaxial nanotubes. *Physica E: Low-dimensional Systems and Nanostructures* **2005**, *28*, 431–438.
- [29] Zhang, H.; Ding, W.; He, K.; Li, M. Synthesis and characterization of crystalline silicon carbide nanoribbons. *Nanoscale research letters* **2010**, *5*, 1264–1271.
- [30] Fan, J.; Wu, X.; Chu, P. K. Low-dimensional SiC nanostructures: fabrication, luminescence, and electrical properties. *Progress in materials science* **2006**, *51*, 983–1031.
- [31] Chen, S.; Li, W.; Li, X.; Yang, W. One-dimensional SiC nanostructures: Designed growth, properties, and applications. *Progress in Materials Science* **2019**, *104*, 138–214.
- [32] Ponraj, J. S.; Dhanabalan, S. C.; Attolini, G.; Salviati, G. SiC nanostructures toward biomedical applications and its future challenges. *Critical Reviews in Solid State and Materials Sciences* **2016**, *41*, 430–446.
- [33] Wei, J.; Li, K.-Z.; Li, H.-J.; Fu, Q.-G.; Zhang, L. Growth and morphology of one-dimensional SiC nanostructures without catalyst assistant. *Materials chemistry and Physics* **2006**, *95*, 140–144.
- [34] Mélinon, P.; Kéghélian, P.; Perez, A.; Ray, C.; Lermé, J.; Pellarin, M.; Broyer, M.; Boudeulle, M.; Champagnon, B.; Rousset, J. Nanostructured SiC films obtained by neutral-cluster depositions. *Physical Review B* **1998**, *58*, 16481.
- [35] Alaal, N.; Loganathan, V.; Medhekar, N.; Shukla, A. First principles many-body calculations of electronic structure and optical properties of SiC nanoribbons. *Journal of Physics D: Applied Physics* **2016**, *49*, 105306.
- [36] Alaal, N.; Loganathan, V.; Medhekar, N.; Shukla, A. From half-metal to semiconductor: Electron-correlation effects in zigzag SiC nanoribbons from first principles. *Physical Review Applied* **2017**, *7*, 064009.
- [37] Chabi, S.; Guler, Z.; Brearley, A. J.; Benavidez, A. D.; Luk, T. S. The Creation of True Two-Dimensional Silicon Carbide. *Nanomaterials* **2021**, *11*, 1799.

- [38] Polley, C.; Fedderwitz, H.; Balasubramanian, T.; Zakharov, A.; Yakimova, R.; Bäcke, O.; Ekman, J.; Dash, S.; Kubatkin, S.; Lara-Avila, S. Bottom-up growth of monolayer honeycomb SiC. *Physical Review Letters* **2023**, *130*, 076203.
- [39] Raffaele, R. P.; Castro, S. L.; Hepp, A. F.; Bailey, S. G. Quantum dot solar cells. *Progress in Photovoltaics: Research and Applications* **2002**, *10*, 433–439.
- [40] Rahman, M. M.; Karim, M. R.; Alharbi, H. F.; Aldokhayel, B.; Uzzaman, T.; Zahir, H. Cadmium Selenide quantum dots for solar cell applications: a review. *Chemistry—An Asian Journal* **2021**, *16*, 902–921.
- [41] Mahalingam, S.; Manap, A.; Omar, A.; Low, F. W.; Afandi, N.; Chia, C. H.; Abd Rahim, N. Functionalized graphene quantum dots for dye-sensitized solar cell: Key challenges, recent developments and future prospects. *Renewable and Sustainable Energy Reviews* **2021**, *144*, 110999.
- [42] Shen, Y.-J.; Lee, Y.-L. Assembly of CdS quantum dots onto mesoscopic TiO<sub>2</sub> films for quantum dot-sensitized solar cell applications. *Nanotechnology* **2008**, *19*, 045602.
- [43] Yan, Y.; Gong, J.; Chen, J.; Zeng, Z.; Huang, W.; Pu, K.; Liu, J.; Chen, P. Recent advances on graphene quantum dots: from chemistry and physics to applications. *Advanced Materials* **2019**, *31*, 1808283.
- [44] Skolnick, M.; Mowbray, D. Self-assembled semiconductor quantum dots: Fundamental physics and device applications. *Annu. Rev. Mater. Res.* **2004**, *34*, 181–218.
- [45] Nann, T.; Skinner, W. M. Quantum dots for electro-optic devices. *Acs Nano* **2011**, *5*, 5291–5295.
- [46] Sun, Q.; Wang, Y. A.; Li, L. S.; Wang, D.; Zhu, T.; Xu, J.; Yang, C.; Li, Y. Bright, multicoloured light-emitting diodes based on quantum dots. *Nature photonics* **2007**, *1*, 717–722.
- [47] Dai, X.; Zhang, Z.; Jin, Y.; Niu, Y.; Cao, H.; Liang, X.; Chen, L.; Wang, J.; Peng, X. Solution-processed, high-performance light-emitting diodes based on quantum dots. *Nature* **2014**, *515*, 96–99.
- [48] Liu, Z.; Lin, C.-H.; Hyun, B.-R.; Sher, C.-W.; Lv, Z.; Luo, B.; Jiang, F.; Wu, T.; Ho, C.-H.; Kuo, H.-C., et al. Micro-light-emitting diodes with quantum dots in display technology. *Light: Science & Applications* **2020**, *9*, 1–23.
- [49] Moon, H.; Lee, C.; Lee, W.; Kim, J.; Chae, H. Stability of quantum dots, quantum dot films, and quantum dot light-emitting diodes for display applications. *Advanced Materials* **2019**, *31*, 1804294.
- [50] Shi, Z.; Li, Y.; Zhang, Y.; Chen, Y.; Li, X.; Wu, D.; Xu, T.; Shan, C.; Du, G. High-efficiency and air-stable perovskite quantum dots light-emitting diodes with an all-inorganic heterostructure. *Nano Letters* **2017**, *17*, 313–321.
- [51] Yao, L.; Yu, T.; Ba, L.; Meng, H.; Fang, X.; Wang, Y.; Li, L.; Rong, X.; Wang, S.; Wang, X., et al. Efficient silicon quantum dots light emitting diodes with an inverted device structure. *Journal of Materials Chemistry C* **2016**, *4*, 673–677.



- [52] Park, N.-M.; Kim, T.-S.; Park, S.-J. Band gap engineering of amorphous silicon quantum dots for light-emitting diodes. *Applied Physics Letters* **2001**, *78*, 2575–2577.
- [53] Veeramani, V.; Bao, Z.; Chan, M.-H.; Wang, H.-C.; Jena, A.; Chang, H.; Hu, S.-F.; Liu, R.-S. Quantum dots for light conversion, therapeutic and energy storage applications. *Journal of Solid State Chemistry* **2019**, *270*, 71–84.
- [54] Cao, Y.; Dong, H.; Pu, S.; Zhang, X. Photoluminescent two-dimensional SiC quantum dots for cellular imaging and transport. *Nano research* **2018**, *11*, 4074–4081.
- [55] Mizuno, T.; Kanazawa, R.; Aoki, T.; Sameshima, T. SiC quantum dot formation in SiO<sub>2</sub> layer using double hot-Si<sup>+</sup>/C<sup>+</sup>-ion implantation technique. *Japanese Journal of Applied Physics* **2020**, *59*, SGGH02.
- [56] Qin, X.; Liu, Y.; Li, X.; Xu, J.; Chi, B.; Zhai, D.; Zhao, X. Origin of Dirac cones in SiC silagraphene: a combined density functional and tight-binding study. *The Journal of Physical Chemistry Letters* **2015**, *6*, 1333–1339.
- [57] Yang, C.; Xie, Y.; Liu, L.-M.; Chen, Y. Versatile electronic properties and exotic edge states of single-layer tetragonal silicon carbides. *Phys. Chem. Chem. Phys.* **2015**, *17*, 11211–11216.
- [58] Long, H.; Hu, J.; Xie, X.; Hu, P.; Wang, S.; Wen, M.; Zhang, X.; Wu, F.; Dong, H. SiC siligraphene: a novel SiC allotrope with wide tunable direct band gap and strong anisotropy. *Journal of Physics D: Applied Physics* **2021**, *54*, 225102.
- [59] Yang, M.; Lian, Z.; Si, C.; Li, B. Revealing the role of nitrogen dopants in tuning the electronic and optical properties of graphene quantum dots via a TD-DFT study. *Physical Chemistry Chemical Physics* **2020**, *22*, 28230–28237.
- [60] Liu, Q.; Sun, J.; Gao, K.; Chen, N.; Sun, X.; Ti, D.; Bai, C.; Cui, R.; Qu, L. Graphene quantum dots for energy storage and conversion: from fabrication to applications. *Materials Chemistry Frontiers* **2020**, *4*, 421–436.
- [61] Sharma, V.; Roondhe, B.; Saxena, S.; Shukla, A. Role of functionalized graphene quantum dots in hydrogen evolution reaction: A density functional theory study. *International Journal of Hydrogen Energy* **2022**, *47*, 41748–41758.
- [62] Sharma, V.; Kagdada, H. L.; Jha, P. K. Four-fold enhancement in the thermoelectric power factor of germanium selenide monolayer by adsorption of graphene quantum dot. *Energy* **2020**, *196*, 117104.
- [63] Qi, W.; Li, M.; Zhao, L. One-step fabrication of photoluminescent SiC quantum dots through a radiation technique. *New J. Chem.* **2020**, *44*, 13301–13307.
- [64] Pan, D.; Zhang, J.; Li, Z.; Wu, M. Hydrothermal route for cutting graphene sheets into blue-luminescent graphene quantum dots. *Advanced materials* **2010**, *22*, 734–738.

- [65] Ge, J.; Lan, M.; Zhou, B.; Liu, W.; Guo, L.; Wang, H.; Jia, Q.; Niu, G.; Huang, X.; Zhou, H., et al. A graphene quantum dot photodynamic therapy agent with high singlet oxygen generation. *Nature communications* **2014**, *5*, 4596.
- [66] Dai, W.; Dong, H.; Fugetsu, B.; Cao, Y.; Lu, H.; Ma, X.; Zhang, X. Tunable fabrication of molybdenum disulfide quantum dots for intracellular microRNA detection and multiphoton bioimaging. *Small* **2015**, *11*, 4158–4164.
- [67] Xi, Y.; Zhao, M.; Wang, X.; Li, S.; He, X.; Wang, Z.; Bu, H. Honeycomb-patterned quantum dots beyond graphene. *The Journal of Physical Chemistry C* **2011**, *115*, 17743–17749.
- [68] Ouarrad, H.; Ramadan, F.; Drissi, L. Engineering silicon-carbide quantum dots for third generation photovoltaic cells. *Optics Express* **2020**, *28*, 36656–36667.
- [69] Benemanskaya, G.; Dementev, P.; Kukushkin, S.; Osipov, A.; Timoshnev, S. Carbon-based aromatic-like nanostructures on the vicinal SiC surfaces induced by Ba adsorption. *ECS Journal of Solid State Science and Technology* **2019**, *8*, M53.
- [70] Xu, Q.; Cai, W.; Li, W.; Sreepasad, T. S.; He, Z.; Ong, W.-J.; Li, N. Two-dimensional quantum dots: Fundamentals, photoluminescence mechanism and their energy and environmental applications. *Materials today energy* **2018**, *10*, 222–240.
- [71] Gundra, K.; Shukla, A. In *Topological Modelling of Nanostructures and Extended Systems*; Ashrafi, A. R., Cataldo, F., Iranmanesh, A., Ori, O., Eds.; Springer Netherlands: Dordrecht, 2013; pp 199–227.
- [72] Rai, D. K.; Shukla, A. Excited States and Optical Properties of Hydrogen-Passivated Rectangular Graphenes: A Computational Study. *Scientific Reports* **2019**, *9*, 7958.
- [73] Basak, T.; Basak, T.; Shukla, A. Graphene quantum dots with a Stone-Wales defect as a topologically tunable platform for visible-light harvesting. *Phys. Rev. B* **2021**, *103*, 235420.
- [74] Camacho-Mojica, D. C.; López-Urías, F. GaN haeckelite single-layered nanostructures: monolayer and nanotubes. *Scientific reports* **2015**, *5*, 1–11.
- [75] Jindal, R.; Sharma, V.; Shukla, A. Density functional theory study of the hydrogen evolution reaction in haeckelite boron nitride quantum dots. *International Journal of Hydrogen Energy* **2022**,
- [76] Frisch, A., et al. gaussian 09W Reference. *Wallingford, USA, 25p* **2009**,
- [77] Hohenberg, P.; Kohn, W. Inhomogeneous electron gas. *Physical review* **1964**, *136*, B864.
- [78] Kohn, W.; Sham, L. J. Self-Consistent Equations Including Exchange and Correlation Effects. *Phys. Rev.* **1965**, *140*, A1133–A1138.
- [79] Jones, R. O.; Gunnarsson, O. The density functional formalism, its applications and prospects. *Rev. Mod. Phys.* **1989**, *61*, 689–746.

- [80] Dennington, R.; Keith, T.; Millam, J., et al. GaussView, version 5. 2009.
- [81] Becke, A. D. Density-functional exchange-energy approximation with correct asymptotic behavior. *Physical review A* **1988**, *38*, 3098.
- [82] Lee, C.; Yang, W.; Parr, R. G. Development of the Colle-Salvetti correlation-energy formula into a functional of the electron density. *Physical review B* **1988**, *37*, 785.
- [83] Tomić, S.; Montanari, B.; Harrison, N. The group III–V’s semiconductor energy gaps predicted using the B3LYP hybrid functional. *Physica E: Low-dimensional Systems and Nanostructures* **2008**, *40*, 2125–2127.
- [84] Garoufalidis, C. S.; Zdetsis, A. D.; Grimme, S. High Level Ab Initio Calculations of the Optical Gap of Small Silicon Quantum Dots. *Phys. Rev. Lett.* **2001**, *87*, 276402.
- [85] Williamson, A. J.; Grossman, J. C.; Hood, R. Q.; Puzder, A.; Galli, G. Quantum Monte Carlo Calculations of Nanostructure Optical Gaps: Application to Silicon Quantum Dots. *Phys. Rev. Lett.* **2002**, *89*, 196803.
- [86] Niaz, S.; Koukaras, E. N.; Katsougrakis, N. P.; Kourelis, T. G.; Kougias, D. K.; Zdetsis, A. D. Size dependence of the optical gap of small silicon quantum dots: Ab initio and empirical correlation schemes. *Microelectronic engineering* **2013**, *112*, 231–234.
- [87] Lu, T.; Chen, F. Multiwfn: a multifunctional wavefunction analyzer. *Journal of computational chemistry* **2012**, *33*, 580–592.
- [88] Martínez, J. Local reactivity descriptors from degenerate frontier molecular orbitals. *Chemical Physics Letters* **2009**, *478*, 310–322.
- [89] Bradley, J.; Gerrans, G. Frontier molecular orbitals. A link between kinetics and bonding theory. *Journal of Chemical Education* **1973**, *50*, 463.
- [90] Kiyooka, S.-i.; Kaneno, D.; Fujiyama, R. Intrinsic reactivity index as a single scale directed toward both electrophilicity and nucleophilicity using frontier molecular orbitals. *Tetrahedron* **2013**, *69*, 4247–4258.
- [91] Kresse, G.; Hafner, J. Ab initio molecular dynamics for liquid metals. *Physical review B* **1993**, *47*, 558.
- [92] Kresse, G.; Furthmüller, J. Efficiency of ab-initio total energy calculations for metals and semiconductors using a plane-wave basis set. *Computational materials science* **1996**, *6*, 15–50.
- [93] Kresse, G.; Furthmüller, J. Efficient iterative schemes for ab initio total-energy calculations using a plane-wave basis set. *Physical review B* **1996**, *54*, 11169.
- [94] Kresse, G.; Joubert, D. From ultrasoft pseudopotentials to the projector augmented-wave method. *Physical review b* **1999**, *59*, 1758.
- [95] Azhagiri, S.; Jayakumar, S.; Gunasekaran, S.; Srinivasan, S. Molecular structure, Mulliken charge, frontier molecular orbital and first hyperpolarizability analysis on 2-nitroaniline and 4-methoxy-2-nitroaniline using density functional theory. *Spectrochimica Acta Part A: Molecular and Biomolecular Spectroscopy* **2014**, *124*, 199–202.

- [96] Jasmine, N. J.; Muthiah, P. T.; Arunagiri, C.; Subashini, A. Vibrational spectra ( experimental and theoretical), molecular structure, natural bond orbital, HOMO–LUMO energy, Mulliken charge and thermodynamic analysis of N<sup>1</sup>-hydroxy-pyrimidine-2-carboximidamide by DFT approach. *Spectrochimica Acta Part A: Molecular and Biomolecular Spectroscopy* **2015**, *144*, 215–225.
- [97] Parr, R. G.; Pearson, R. G. Absolute hardness: companion parameter to absolute electronegativity. *Journal of the American chemical society* **1983**, *105*, 7512–7516.
- [98] Pearson, R. G. Absolute electronegativity and hardness correlated with molecular orbital theory. *Proceedings of the National Academy of Sciences* **1986**, *83*, 8440–8441.
- [99] Pearson, R. G. Chemical hardness and the electronic chemical potential. *Inorganica chimica acta* **1992**, *198*, 781–786.
- [100] Aihara, J.-i. Reduced HOMO- LUMO gap as an index of kinetic stability for polycyclic aromatic hydrocarbons. *The Journal of Physical Chemistry A* **1999**, *103*, 7487–7495.
- [101] Pandey, D. K.; Kagdada, H. L.; Materny, A.; Singh, D. K. Hybrid structure of ionic liquid and TiO<sub>2</sub> nanoclusters for efficient hydrogen evolution reaction. *The Journal of Physical Chemistry A* **2021**, *125*, 2653–2665.
- [102] Soos, Z.; Ramasesha, S. Valence-bond theory of linear Hubbard and Pariser-Parr-Pople models. *Physical Review B* **1984**, *29*, 5410.
- [103] Basak, T.; Chakraborty, H.; Shukla, A. Theory of linear optical absorption in diamond-shaped graphene quantum dots. *Physical Review B* **2015**, *92*, 205404.